Article

Investigation on Film Formation Characteristics of Pressure-Swirl Nozzle

Dongyun Ma [1], Shinan Chang [1],* and Chen Yang [2],*

[1] School of Aeronautic Science and Engineering, Beihang University, Beijing 100191, China; madongyun@buaa.edu.cn
[2] Qian Xuesen Laboratory of Space Technology, China Academy of Space Technology, Beijing 100094, China
* Correspondence: sn_chang@buaa.edu.cn (S.C.); yangchen@qxslab.cn (C.Y.)

Abstract: The film formation during the spray/wall impingement has attracted more attention. The present study investigated the film formation characteristics of the pressure-swirl nozzle by applying the contact-free optical method. According to experimental results, the impingement distance had a slightly more significant effect on the actual spray angle than the mass flow rate, and the maximum changing value was 34.6°. The bulge at the center of the surface became insignificant with the impingement distance. The liquid film was divided into the raised zone, annular zone, and free flow zone. The maximum time-average thickness at the central position was 2.84 mm, and correlations for predicting the time-average thickness and surface roughness were fitted. The time-average thickness of the annular zone was 0.38–0.59 mm, relatively thinner than other zones. When the impingement distance was lower than 10 mm, the time-average film thickness and surface roughness in the annular zone and free flow zone decreased first and then increased with the impingement distance. However, effects of mass flow rates and impingement distance on the liquid film were negligible when the impingement distance was higher than 10 mm. The experimental findings are helpful to fundamentally understand the film formation during the spray/wall impingement.

Keywords: film formation; pressure-swirl nozzle; radial distribution; spray/wall impingement

1. Introduction

The spray impingement onto walls is a typical phenomenon in combustion, coating, anti-icing, and spray cooling [1,2]. When the droplets attached to walls cannot completely evaporate, a liquid film is formed. Recent efforts have been made to the spray/wall impingement, particularly the liquid film characteristics. However, the spray/wall impingement is a complex multiphase flow process (solid-liquid-gas interaction), and the hydrodynamics of the spray/wall impingement is not the statistical superposition of behaviors of a single droplet impingement due to the droplet interaction [3–6]. Furthermore, the spray impingement/wall is affected by many factors, such as the impingement distance and angle, the working liquid and wall temperature, the gas pressure and temperature, etc. [7,8]. Identifying the main parameter is difficult and the universal correlations of the spray/wall impingement have not been approved to a large extent. Therefore, the challenge in interpreting the spray/wall impingement has always attracted more attention [9–11].

As a simplex nozzle, the pressure-swirl nozzle is widely applied because of the good atomization and geometrical simplicity [12]. For the spray/wall impingement with a pressure-swirl nozzle, a hollow spray is generated in the external flow near the nozzle outlet due to the air core inside the swirl chamber [13–15]. The hollow zone of the spray is called the entrainment zone, and the air and droplets fill the entrainment zone where the droplet velocity is negative owing to the entrainment of the induced air [16–18]. The radial maldistribution in the external flow of the spray generated by pressure-swirl nozzles was observed by Chen et al. [19]. They found that the mass flow rate was low near the center of the spray and most of droplets were concentrated near the periphery. In addition, the

influence of the air core becomes weak as droplets move downstream. When the rectifying effect of the air core is insufficient to maintain the negative pressure in the entrainment zone, the hollow cone collapses and forms the full cone spray [20].

Therefore, the air entrainment depending on the impingement distance might play an important role in the film formation during the spray/wall impingement with a pressure-swirl nozzle. Although many researchers have paid enough attention to the liquid film, the effects of the air entrainment on the radial distribution of the surface topography and film thickness are not interpreted in detail [21,22]. In the present study, the experimental work with a pressure-swirl nozzle was performed in a wide range of impingement distances and mass flow rates. And the contact-free optical diagnosis method was applied to investigate temporal and time-average film characteristics on a flat surface. The present study is conductive to fundamentally understand the film formation characteristics during the spray/wall impingement.

2. Methods

2.1. Experimental Setup

Figure 1 shows the experimental apparatus including the fluid system and the contact-free measurement system. The fluid system mainly consisted of the water tank (a, Hongli Co., Foshan, China), the filter (b, Shentong Co., Nanjing, China), the micropump (c, Huyue Co., Taizhou, China), the valve (d, Hanyuxuan Co., Tangshan, China), the flowmeter (accuracy of 2.5%, Zhentai Co., Changshu, China) (e), and the pressure-swirl nozzle (Feizhuo-FN3-ss, full-cone nozzle, orifice diameter of 0.46 mm, Shanghai, China) (f). The contact-free measurement system was composed of the high speed CCD camera (g, Photron Co., San Diego, CA, USA), the Nd:YAG solid-state laser (single wavelength of 532 nm, Cube-world Co., Beijing, China) (h), the controller (i, Cube-world Co., Beijing, China), and the computer (j, Dell Co., Round Rock, TX, USA).
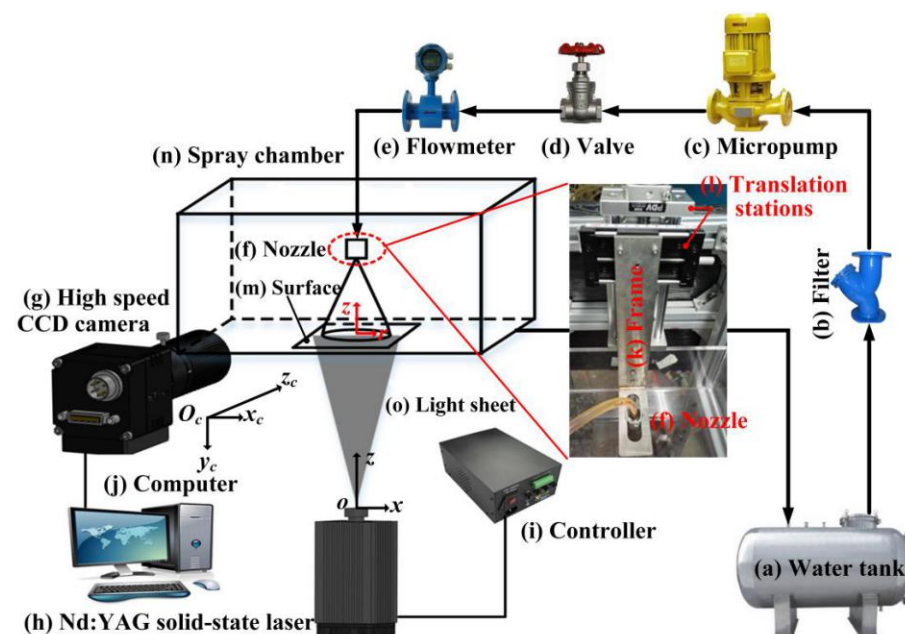

Figure 1. Experimental setup of studying the film formation with the pressure-swirl nozzle.

2.1.1. Fluid System Description

Before experimenting, mixed solutions of different concentrations composed of the working liquid and fluorescent dye (Rhodamine 6G, Maikun Chemical Co., Shanghai, China) were prepared. Via the comparison of liquid film images, the concentration of the Rhodamine 6G was determined as 1 mg/L. And then the working liquid mixed with the Rhodamine 6G was forced by the hydraulic pressure to sequentially flow through (b), (d),

and (e), and finally enter (f). The nozzle was fixed on an L-shaped frame (k) and installed perpendicular to the flat surface made of the transparent plexiglass (30 mm × 30 mm) (m). In addition, (k) was jointed with the horizontal and vertical translation stages (l) to adjust the relative position between (f) and (m) during performing experiments. Thereafter, the working liquid was atomized. Droplets moved downstream and impinged onto (m). For purposes of protecting (g) and reusing the working liquid, the transparent spray chamber (400 mm × 300 mm ×150 mm) (n) with a discharge hole was manufactured.

2.1.2. Contact-Free Measurement System

As shown in Figure 1, (h) was located at the bottom of (n). After the laser spot passed through the plano-concave lens which was mounted on the front of the laser, the laser beam became the light sheet (o) and entered the liquid film. The final width of the light sheet projected onto the flat surface was about 8 cm, and the measured liquid film was located in the center zone of the projected light during experimenting. In addition, the laser was a pulsed one, and the power, pulse duration, energy, and repetition rate were set to 2.5 w, 8 ns, 200 mJ, and 10 Hz, respectively. (o) coincided with the axial cross section of the spray by adjusting the position of the laser. (g) was fixed in front of (n) and the optical axis of the camera was orthogonal to (o). The fluorescent signal emitted from the liquid film when (o) entered the liquid film was collected by the camera. A filter lens (wavelength of 550 nm) was chosen to reduce the influence of the ambient light. And a macro lens (focal length of 100 mm) was applied to realize the close-up shooting since the liquid film was thin and fluctuating. The frame, resolution, and exposure time of the camera were 4000 fps, 1280 pixels × 1024 pixels, and 1/8000 s, respectively. Besides, some shading measures were taken and the experimental work was performed at night to avoid the interference coming from the ambient light.

2.2. Post-Processing Steps of Extracting Film Edges

The image of a standard ruler was recorded before experimenting, and a pixel measured 0.03 mm for the present resolution of the high speed CCD camera. Thereafter, a series of post-processing steps were performed to deal with liquid film images. Figure 2 shows the detailed process of extracting the upper edge of the liquid film, as follows: (a) the image was first appropriately cropped to improve the processing speed (from 1280 pixels × 1024 pixels to 1280 pixels × 180 pixels); (b) the filtering process was performed by wavelet transform (bior5.5) to reduce the gray value step between adjacent pixels in the image; (c) the horizontal blur was chosen to further reduce the singularity value of a single pixel in the image; (d) grayscale stretching and binary of the image were applied, and the gray threshold was determined as 0.5; (e) the upper edge of the liquid film was extracted by adopting the Sobel operator; (f) the iterative step was programmed and the final upper edge of the liquid film was recorded when the pixel difference between two iterations was less than 1 pixel.

In addition, the lower edge of the liquid film was obtained by applying the linear fitting method which reduced the influence of the surface unevenness on measurement results. Extracting 10 values of pixel coordinates on the plexiglass surface without the liquid film, a baseline was obtained by fitting extracted pixel coordinates, which was the lower edge of the liquid film. The deviation of the linear fitting process was less than 1 pixel. Therefore, the pixel value corresponding to the liquid film thickness was obtained by calculating the pixel difference of the upper and lower edges of the liquid film at the same position. The final uncertainty of post-processing steps of liquid film images was within 2 pixels, thus, making the uncertainty less than 0.06 mm.
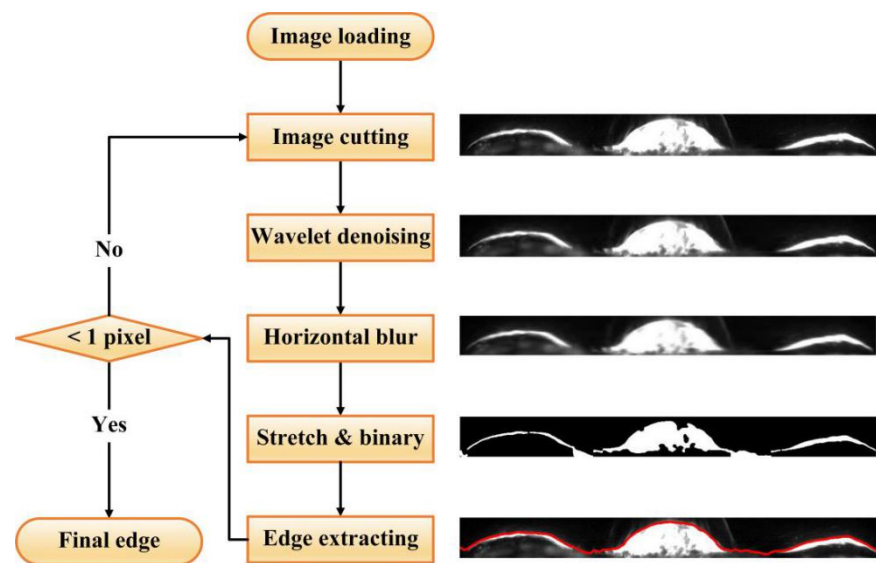
Figure 2. Post-processing steps of extracting the upper edge of the liquid film.

2.3. Experimental Conditions

Pure water was chosen as the working fluid in the present study. On one hand, the pure water with good chemical stability was innocuous and easily available. On the other hand, the water film generated by pressure-swirl nozzles (TG4 and TG6, Spray Co., Glendale Heights, IL, USA) was investigated by Chen et al. [19] by applying the invasive method. However, the needle inevitably introduced some interference into the liquid film during experimenting, which might lead to inaccurate measurement results. Besides, the time-average film thickness at the impingement distance of 10 and 15 mm was the only measurement, and the significant influence of the impingement distance and mass flow rate was not observed.

As mentioned in Section 1, the air entrainment was related to the impingement distance. Therefore, to further explore the influence of the air entrainment on the film formation during the spray/wall impingement and to compare with the published study [19], the pure water was determined as the working fluid, and the impingement distance was in a relatively wider range of 8–30 mm. 35 experimental conditions were listed in Table 1.

Table 1. Experimental conditions.

No.	q (mL/min)	h (mm)
Cases 1–7	100	
Cases 8–14	120	
Cases 15–21	150	5, 8, 10, 15, 20, 25, 30
Cases 22–28	170	
Cases 29–35	190	
Experimental temperature: $(28.5 \pm 0.5)\,°C$		

q is the mass flow rates, h is the impingement distance.

3. Results

3.1. Actual Spray Angle

The droplets are subjected to the aerodynamic resistance, viscous force, surface tension, and inertial force when moving downstream. Therefore, the spray boundary is shrinking as the impingement distance increases, and the actual coverage of the spray is smaller than the theoretical coverage. The actual spray angle, α_h is usually introduced and defined as the full cone angle with the fluid at the nozzle exit [23,24]. In the present study, the actual spray angle

was measured from slopes of the spray boundary of the liquid film image. Figure 3 presents variations of the actual spray angle under experimental conditions. As seen from Figure 3a, the actual spray angle decreased with the impingement distance, and changing values were in the range of 16.4°–24.3°. Moreover, changes in the actual spray angle were more obvious as the impingement distance increased from 8 to 10 mm. The actual spray angle increased with the mass flow rate, and the maximum changing value was 34.6°. However, the changes became gradually insignificant with the further increase of the impingement distance. As found from Figure 3b, changing values of the actual spray angle at a fixed mass flow rate increased when the impingement distance varied from 5 to 30 mm.
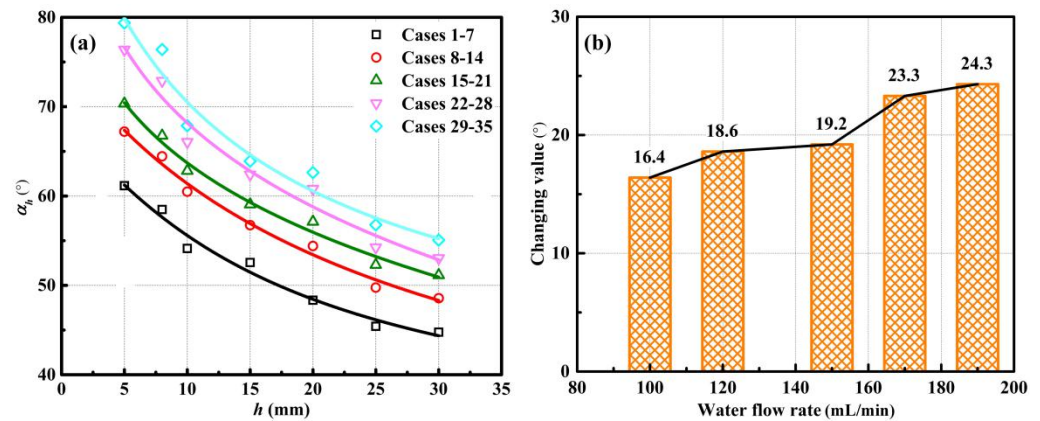

Figure 3. Actual spray angles of the pressure-swirl nozzle, (**a**) variations of the actual spray cones with the impingement distance, (**b**) changing values of the actual spray angles at a fixed mass flow rate.

3.2. Temporal Characteristics

3.2.1. Temporal Film Topography

Figure 4 shows the temporal film topography under different experimental conditions after the binary processing of liquid film images. As seen, the radial distribution of the liquid film on the flat surface was non-uniform, and the film thickness varied with the increase of the radial distance. The bulge phenomenon at the center of the surface was observed, which was not observed in the previous work of Chen et al. [19]. As the impingement distance increased, the edge of the central bulge became difficult to identify. Due to the negative pressure, droplets were entrained by the induced air into the entrainment zone in the external flow of the pressure-swirl nozzle. Therefore, the projected light sheet was scattered when passing through the entrainment zone in which the air and droplets were mixed, causing the fluorescent signal to be stronger than other positions. The air entrainment was weak, further increasing the impingement distance. Thus, droplets moved downward and impinged onto the surface under the action of inertial force, and the bulge phenomenon was no longer obvious.
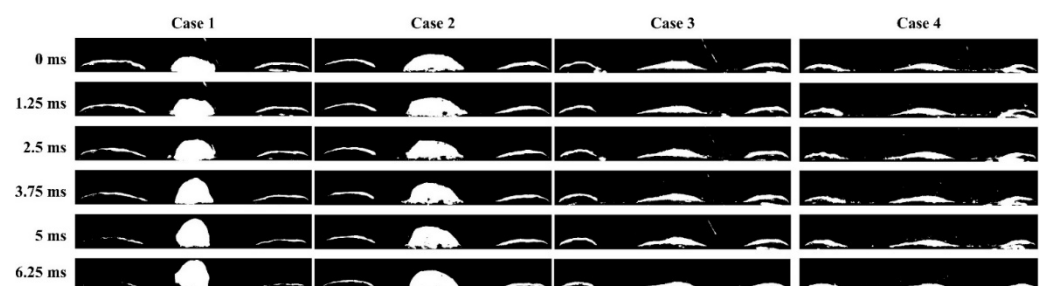

Figure 4. Temporal film topography under different experimental conditions.

In addition, the maximum height of the bulge significantly changed over time at the impingement distance of 5 mm. And the variations of the maximum bulge height

with time were still observed when the impingement distance was 8 mm. However, the maximum bulge height seemed to be constant with further increasing the impingement distance. It was inferred that the formation of the bulge phenomenon was related to the air entrainment, and affected by the negative pressure near the entrainment zone and droplets inertia. When the influence of the negative pressure was more effective than droplets inertia, the bulge height increased. Otherwise, the bulge gradually collapsed.

3.2.2. Temporal Film Thickness

According to the post-processing steps of liquid film images mentioned above, the pixel difference between the upper and lower edges of the liquid film was obtained. And then the product of the pixel difference and the actual distance measured by a single pixel was applied to calculate the temporal film thickness.

Figure 5 shows variations of the temporal film thickness. As seen from Figure 5a–c, variations of the temporal film thickness at different radial positions were different. The liquid film at $r = 0$ mm is fluctuating, and changes in the film thickness were periodical. The transient film thickness at $r = 5$ mm was the thinnest, and some peak values of the film thickness were observed, which were caused by the fluorescence emitted by airborne droplets. For the liquid film at $r = 12$ mm, changes in the film thickness were not obvious. The experimental finding indicated that not only was the film topography but the wave of the liquid film was also different along the radial direction.
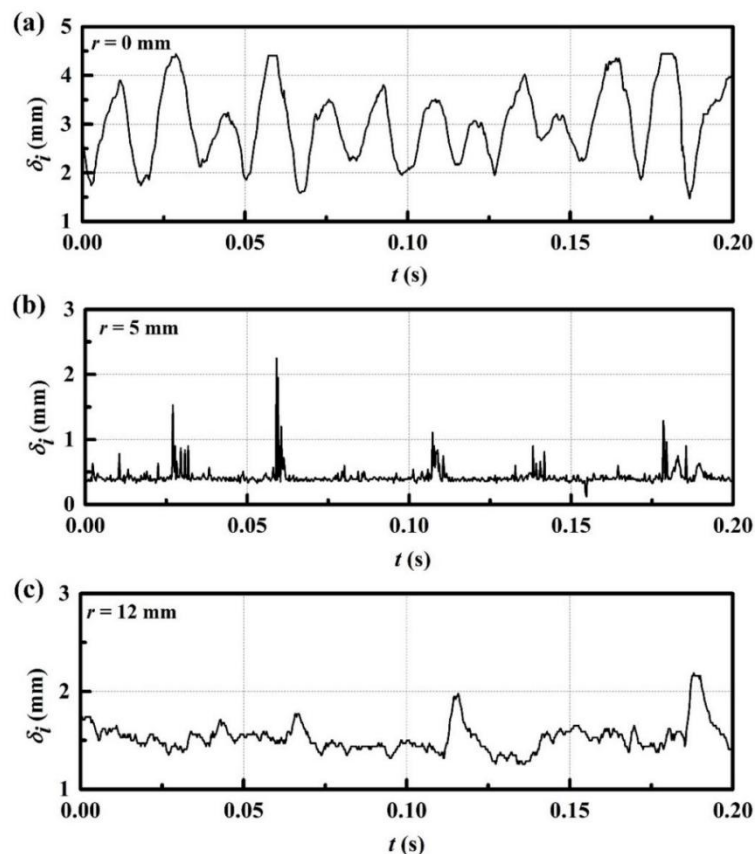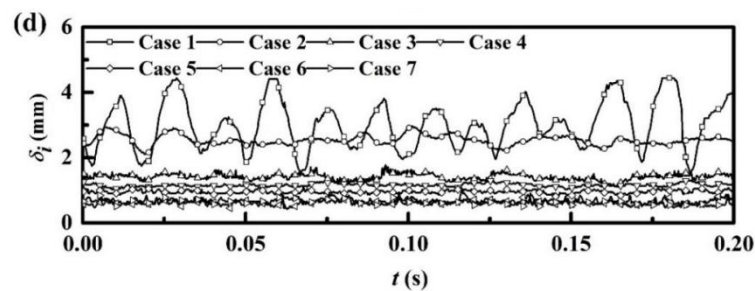

Figure 5. *Cont.*

Figure 5. Temporal film thickness under different experimental conditions. (**a**) variations of the temporal film thickness at r = 0 mm, (**b**) variations of the temporal film thickness at r = 5 mm, (**c**) variations of the temporal film thickness at r = 12 mm, (**d**) variations of the temporal film thickness at r = 0 mm in Cases 1~7.

Figure 5d gives variations of the temporal film thickness at r = 0 mm in Cases 1~7. As shown, the wave of the liquid film was gradually insignificant with the increase of the impingement distance. The bulge recurrently developed and was periodically destructed and re-established under the action of the air entrainment and droplets inertia. However, the air entrainment became weak and droplets impinged onto the surface instead of being entrained by the induced air into the entrainment zone when the impingement distance was always increasing. Besides, the edge perimeter of the bulge was longer according to Figure 4, causing the working liquid in the entrainment zone to be easier to discharge from the bulge. Therefore, the bulge phenomenon was indistinct when the negative pressure in the entrainment zone could be no longer maintained. The wave of the liquid film resulted from the droplet impingement, not the periodic change in the bulge height.

3.3. Time-Average Characteristics

Since temporal characteristics of the liquid film were random, statistical methods were applied to further analyze time-average characteristics. Figure 6 shows variations of the time-average film thickness along a radial direction. As seen, the time-average film thickness was non-uniform in the radial distribution. The liquid film was the thickest at r = 0 mm, and the film thickness gradually decreased with the increase of the radial distance. Thereafter, the time-average film thickness increased first and then decreased along the radial direction again. The experimental result was not consistent with the previous study [19] in which the change in the film thickness was insignificant. In Figure 6a, the influence of the mass flow rate on the radial distribution of the liquid film was negligible. According to Figure 3, the actual spray angle increased with the mass flow rate. However, the actual coverage of the spray at the impingement distance of 5 mm was small. Thus, changes in the actual spray angle had slight effects on the radial distribution of the liquid film. Variations of the time-average film thickness in Figure 6b were similar to Figure 6a. And the significant influence that the impingement distance had on the radial distribution of the liquid film was observed. The time-average film thickness at r = 0 mm decreased with the impingement distance, which was consistent with the film topography in Figure 4. Moreover, positions of the second increase in the time-average film thickness moved to the periphery of the surface. As the impingement distance increased, changes in the actual spray angle were relatively more significant. And the actual coverage of the liquid film increased. When the impingement distance was more than 10 mm, the effects of the impingement distance on the liquid film were negligible.
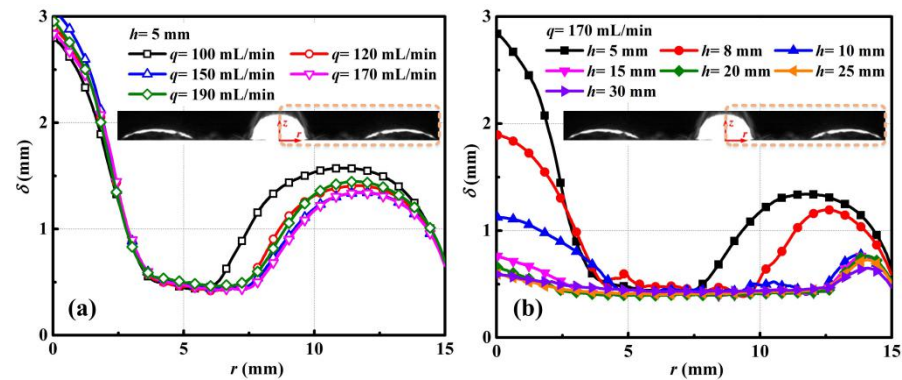
Figure 6. Time-average film thickness along the radial direction of the surface, (**a**) variations of the time-average film thickness under different mass flow rates, (**b**) variations of the time-average film thickness under different impingement distances.

4. Discussion

According to the film topography and radial distribution characteristics of the time-average film thickness, the liquid film was divided into the raised zone, the annular zone, and the free flow zone, as shown in Figure 7. The formation of the raised zone was related to the air entrainment in the external flow of the pressure-swirl nozzle, and became indistinct with the increase of the impingement distance. The momentum of droplets entering into the liquid film is discomposed into the axial and radial components. The axial momentum is converted into the static pressure in the liquid film. And the radial momentum drives the liquid film to flow along the surface. For the annular zone, the pressure gradient within the liquid film is sufficient to overcome the viscous force and surface intensity. Therefore, the working liquid flows away without a stay, causing the liquid film in the annular zone to be relatively thinner. The radial driving force becomes insufficient as the interaction distance the liquid film has with the surface increases, forming the camelback free flow zone. When the liquid film develops outward and flows out of the actual coverage of the spray, the influence of the droplet impingement becomes weak as the increase of radial distance. Therefore, the film formation characteristics during the spray/wall impingement are varied with the radial position on the surface.
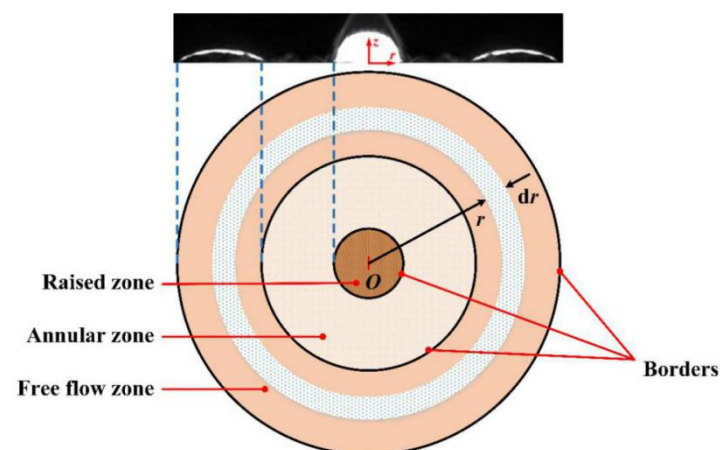

Figure 7. Divided zones of the liquid film according to radial distribution characteristics.

4.1. Film Coverage Rate

The film coverage rate is introduced to study divided zones distribution of the liquid film under experimental conditions, and calculated as follows,

$$\Lambda = \frac{2\pi \int r \mathrm{d}r}{S} \tag{1}$$

where, $2\pi \int r \mathrm{d}r$ and S are areas of the divided zones and the surface, respectively.

Figure 8 shows variations of the film coverage rate. As seen, film coverage rates of the raised zone were smaller than other zones, increasing first and then decreasing with the impingement distance. However, the influence of the mass flow rate was insignificant. It was proposed that the film coverage of the raised zone was related to the air entrainment and actual spray angle. Film coverage rates of the free flow zone were the largest and decreased with the mass flow rate and impingement distance. The film coverage rate of the annular zone was obtained according to the raised zone and free flow zone and was affected by the actual coverage of the spray and the droplet impingement.
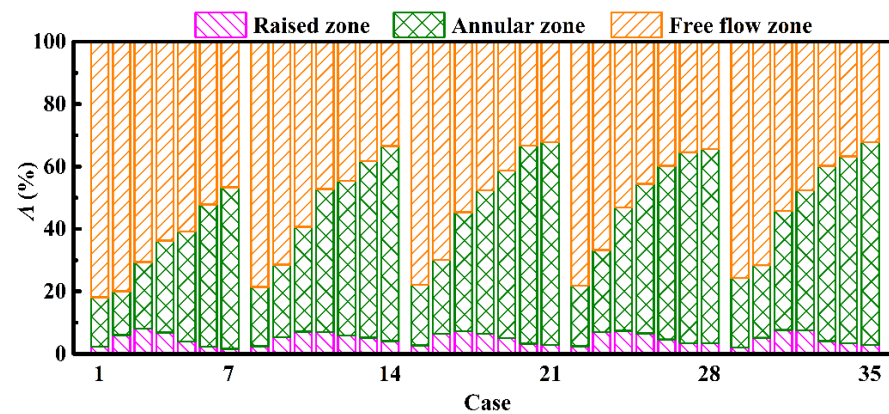

Figure 8. Variations of film coverage rates of different divided zones.

4.2. Raised Zone

According to characteristics of the temporal film topography and thickness in Figures 4 and 5, variations of the border perimeter of the raised zone were studied, as given in Figure 9. The black line was obtained by fitting the data in Cases 1–35, and indicated the changing trend of the border perimeter in the raised zone. As the impingement distance increased, the border perimeter increased first and then decreased. There was a critical impingement distance at which the border perimeter was the longest. Besides, differences in the border perimeter with the mass flow rate were more significant when the impingement distance was higher than 10 mm. Since the bulge phenomenon was no longer obvious, droplets directly impinged into the liquid film. Therefore, the raised zone became insignificant and it was difficult to distinguish the border between the raised zone and the annular zone.

Figure 10 shows variations of the liquid film thickness of the raised zone. As given in Figure 10a, the time-average film thickness at $r = 0$ mm, which was also the maximum film thickness, decreased with the impingement distance. The experimental data was fitted to be the exponential function, as follows:

$$\delta = 0.523 + 6.469e^{-0.19h} \tag{2}$$

where δ is the time-average film thickness.

The maximum deviation was 0.614 mm in Case 30. And changes in the time-average thickness with the mass flow rate were negligible when the impingement distance was higher than 10 mm according to the 95% confidence band and the 95% prediction band.

Therefore, the fitted correlation might be applied to predict the time-average film thickness when the bulge phenomenon was insignificant.

As an important statistical parameter, the root means square (RMS) of the liquid film thickness was used to analyze the average amplitude and evaluate the surface roughness of the wavy liquid film. The RMS in Cases 1–35 was shown in Figure 10b. Similarly, the fitted correlation satisfied the exponential function, as follows:

$$\text{RMS} = 0.046 + 14.3e^{-0.609h} \tag{3}$$

The maximum deviation was 0.089 mm in Case 30. And changes in RMS were insignificant when the impingement distance was higher than 10 mm, which implied that the surface wave was not obvious. The experimental findings were consistent with Figure 5d. According to the 95% confidence band and the 95% prediction band, the fitted correlation was appropriate to evaluate the surface roughness of the wavy liquid film.
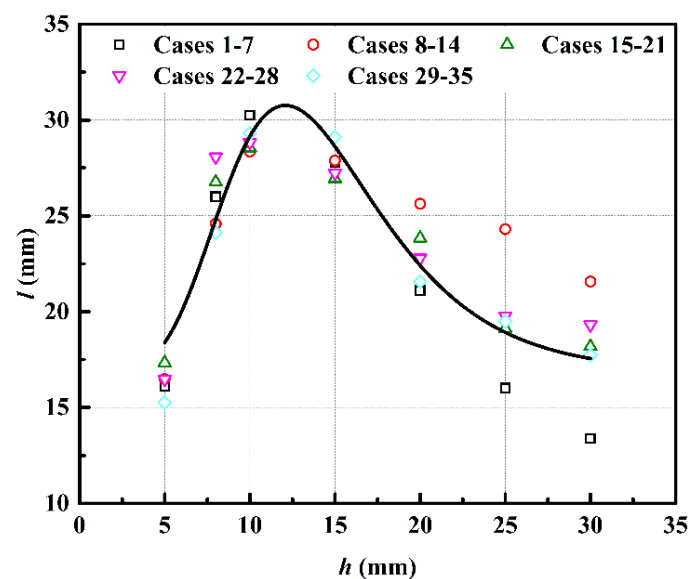

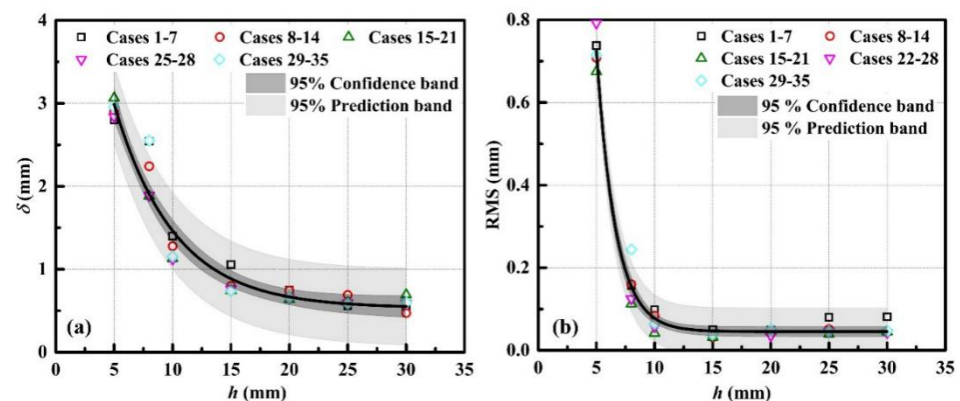**Figure 9.** Variations of the border perimeter of the raised zone.

Figure 10. Variations of the liquid film thickness at $r = 0$ mm. (**a**) variations of the time-average film thickness, (**b**) variations of the RMS in Cases 1–35.

4.3. Annular Zone

As given in Figure 11, variations of the time-average film thickness and RMS at $r = 5$ mm were constructed. As mentioned above, the black lines were the fitted lines for the data in Cases 1–35. The time-average film thickness was 0.38–0.59 mm in Figure 11a.

Although the dynamics within the annular zone were sufficient to drive the liquid film to radially flow without staying, there was still a thin film due to the viscous force. The experimental results indicated that the mass flow rate had a slight effect on the time-average film thickness. However, the effects of the impingement distance were obvious. As found, the time-average film thickness increased first and then decreased with the impingement distance, and the liquid film was relatively thicker when the impingement distance was 8 mm. Moreover, the time-average film thickness increased again when the impingement distance was higher than 10 mm. The reason was that the droplet impingement became weak with the further increase of the impingement distance. And then the liquid film was thicker.
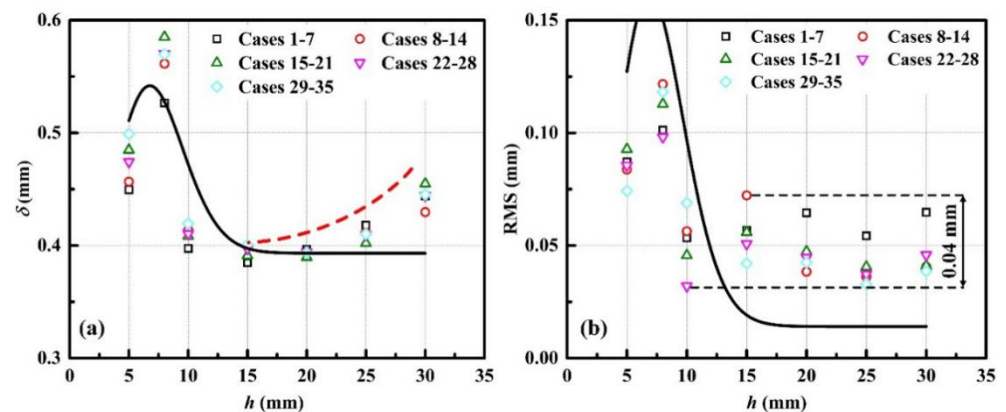

Figure 11. Variations of the liquid film thickness at r = 5 mm. (**a**) variations of the time-average film thickness, (**b**) variations of the RMS in Cases 1–35.

The RMS was analyzed to further study the surface wave, as shown in Figure 11b. The RMS was in the range of 0.03–0.12 mm, and the maximum RMS was 0.12 mm in Case 9. The RMS increased first and then decreased, showing that the surface wave of the liquid film was more intense when the impingement distance was 8 mm. In addition, the maximum difference of RMS under different experimental conditions was 0.04 mm when the impingement distance was higher than 10 mm, which was less than the uncertainty of image post-processing steps. Therefore, the mass flow rate and impingement distance had a slight influence on the wavy liquid film.

4.4. Free Flow Zone

The free flow zone is beyond the actual coverage of the spray during the spray/wall impingement, and thus there is hardly direct droplet impingement and the radial dynamics is only the pressure gradient within the liquid film. When the surface tension and the viscous force are balanced with the radial dynamics, a stagnation point is formed where the liquid film is the thickest. Since the droplet momentum varies with the mass flow rate and impingement distance, the positions of the stagnation point are also different. Figure 12 shows variations of the time-average film thickness and RMS at the stagnation point of the free flow zone. As seen from Figure 12a, the time-average film thickness increased first and then decreased with the impingement distance. The influence of the mass flow rate was negligible except for the 100 mL/min within the uncertainty of image post-processing steps. Moreover, the time-average film thickness was slightly decreased with the impingement distance. The droplet impingement became weak with the increase of the impingement distance. Therefore, the working liquid forced by radial dynamics to flow into the free flow zone decreased, causing the liquid film to be thinner.
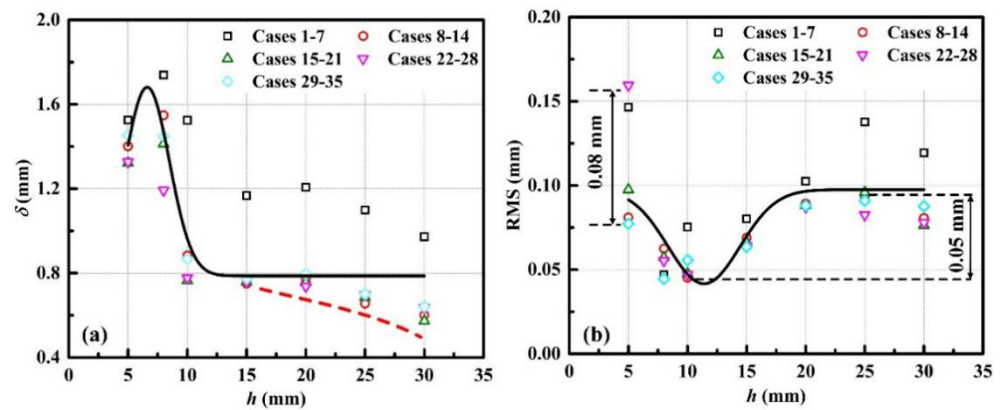
Figure 12. Variations of the liquid film thickness at stagnation points. (**a**) variations of the time-average film thickness, (**b**) variations of the RMS in Cases 1–35.

As seen from Figure 12b, the maximum value of RMS was 0.16 mm in Case 22, and the minimum value was 0.04 mm in Case 10. Values of RMS decreased first and then increased with the increase of the impingement distance. And differences under different mass flow rates were insignificant except 100 mL/min. The maximum difference was 0.05 mm when the impingement distance was higher than 10 mm, which was less than the uncertainty of image post-processing steps. Therefore, the effects of the mass flow rate and impingement distance were negligible.

4.5. Comparison with the Published Study

The liquid film formed during the spray/wall impingement was investigated by Chen et al. [19]. Experimental results showed that no significant changes in the time-average film thickness were observed when impingement distances were 10 and 15 mm. Moreover, they considered that the radial distribution of the film thickness was constant and did not vary along the radial direction of the surface. Therefore, the comparison between the present study and the published study was conducted to provide some references for further work.

Since there were some differences in experimental conditions, related parameters were processed to be dimensionless. The mass flow rate was converted to the Reynolds number at the nozzle outlet, as follows:

$$Re = \frac{4\rho q}{\pi \mu d} \qquad (4)$$

where, $\mu = \frac{4q}{\pi d^2}$ is the velocity at the nozzle outlet, and d is the orifice diameter of the pressure-swirl nozzle, Re is the Reynolds number at the nozzle outlet, d is the orifice diameter of the pressure-swirl nozzle, μ is the viscosity of the pure water. Figure 13 gives the comparison between the previous and present studies. As seen, the time-average film thickness in the present study was significantly thicker and RMS was approximate to values of the time-average film thickness in the published study. For the point gauge method, the time-average film thickness was calculated according to the resistance difference which was caused by the surface wave of the liquid film. Therefore, it was inferred that the time-average film thickness measured by Chen et al. [19] was RMS of the wavy liquid film. Besides, the difference of RMS under different Reynolds numbers at the nozzle outlet was not obvious. According to Figures 11b and 13, RMS could be regarded as constant when the impingement distance was higher than 10 mm regardless of the mass flow rate.
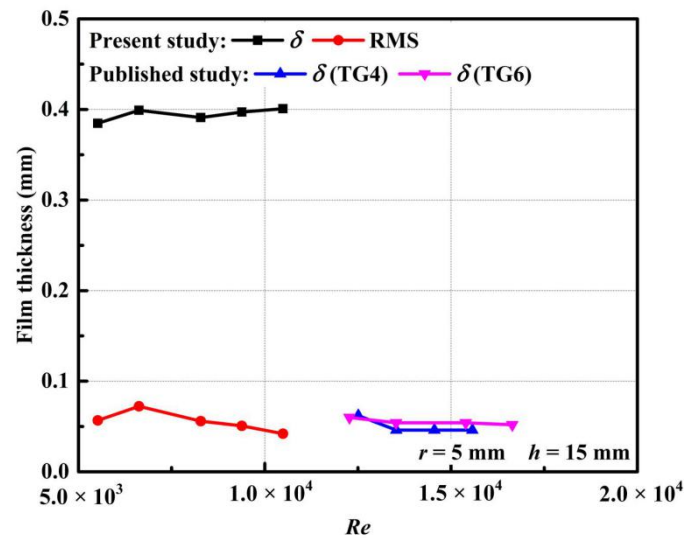
Figure 13. Comparison between the present study and published study.

5. Conclusions

The film formation during the spray/wall impingement was investigated by the contact-free measurement method and statistical methods. The experimental work was performed in a wide range of mass flow rates (100–190 mL/min) and impingement distances (5–30 mm). Some valuable findings were obtained, as follows:

1. The bulge phenomenon on the surface was obvious when the impingement distance was lower than 10 mm, and became indistinct with the further increase of the impingement distance. The correlations predicting the time-average film thickness and RMS at the central position of the surface were fitted.
2. The film thickness was not constant along the radial direction, and the liquid film was divided into the raised zone, annular zone, and free flow zone. Effects of the impingement distance and mass flow rate on the liquid film of the annular zone and free flow zone were negligible when the impingement distance was higher than 10 mm.
3. The influence of the air entrainment on the film formation during the spray/wall impingement was complicated and correlated with experimental conditions. Further work will be conducted to study other factors including fluid characteristics and surface conditions to thoroughly understand the spray/wall impingement.

References

1. Yonemoto, Y.; Kunugi, T. Universality of droplet impingement: Low-to-high viscosities and surface tensions. *Coatings* **2018**, *8*, 409. [CrossRef]
2. Lin, D.; Zhang, L.; Yi, M.; Wang, X.; Gao, S.; Yang, Y.; Wang, X.D. Rebound dynamics of two droplets successively impacting an inclined surface. *Coatings* **2020**, *10*, 592. [CrossRef]
3. Breitenbach, J.; Roisman, I.V.; Tropea, C. From drop impact physics to spray cooling models: A critical review. *Exp. Fluids* **2018**, *59*, 1–21. [CrossRef]
4. Wang, C.; Chang, S.; Leng, M.; Wu, H.; Yang, B. A two-dimensional splashing model for investigating impingement characteristics of supercooled large droplets. *Int. J. Multiph. Flow* **2016**, *80*, 131–149. [CrossRef]
5. Chashechkin, Y.; Prokhorov, V. Drop impact hydrodynamics: Short waves on a crown surface. *Dokl. Phys.* **2013**, *58*, 296–300. [CrossRef]
6. Chashechkin, Y.; Ilinykh, A. Capillary waves on the surface of a droplet falling into a liquid. *Dokl. Phys.* **2015**, *465*, 434–440. [CrossRef]
7. Li, X.; Pan, H.; Dong, X.; Hung, D.; Xu, M. Spray impingement wall film breakup by wave entrainment. *Proc. Combust. Inst.* **2019**, *37*, 3287–3294. [CrossRef]
8. Yu, H.; Liang, X.; Shu, G.; Wang, X.; Wang, Y.; Zhang, H. Experimental investigation on wall film distribution of dimethyl ether/diesel blended fuels formed during spray wall impingement. *Energies* **2016**, *9*, 949. [CrossRef]
9. Choi, K.; Lee, D.; Roh, H.G.; Lee, C.S. Effect of injection parameters on spray characteristics of gas-to liquid (GTL), biodiesel, and diesel fuel for a multi-hole injection in a diesel engine. *At. Sprays* **2015**, *25*, 1107–1125. [CrossRef]
10. Wu, S.; Meinhart, M.; Petersen, B.; Yi, J.; Wooldridge, M. Breakup characteristics of high speed liquid jets from a single-hole injector. *Fuel* **2021**, *289*, 119784. [CrossRef]
11. De la Garza, O.A.; Martínez-Martínez, S.; Avulapati, M.M.; Pos, R.; Megaritis, T.; Ganippa, L. Biofuels and its spray interactions under pilot-main injection strategy. *Energy* **2021**, *219*, 119464. [CrossRef]
12. Som, S.K. Air core in pressure swirl atomizing nozzles. *At. Sprays* **2012**, *22*, 283–303. [CrossRef]
13. Vijay, G.A.; Moorthi, N.S.V.; Manivannan, A. Internal and external flow characteristics of swirl atomizers: A review. *At. Sprays* **2015**, *25*, 153–188. [CrossRef]
14. Lee, E.J.; Oh, S.Y.; Kim, H.Y.; James, S.C.; Yoon, S.S. Measuring air core characteristics of a pressure-swirl atomizer via a transparent acrylic nozzle at various Reynolds numbers. *Exp. Therm. Fluid Sci.* **2010**, *34*, 1475–1483. [CrossRef]
15. Datta, A.; Som, S.K. Numerical prediction of air core diameter, coefficient of discharge and spray cone angle of a swirl spray pressure nozzle. *Int. J. Heat Fluid Flow* **2000**, *21*, 412–419. [CrossRef]
16. Cossali, G.E. An integral model for gas entrainment into full cone sprays. *J. Fluid Mech.* **2001**, *439*, 353–366. [CrossRef]
17. Moon, S.; Matsumoto, Y.; Nishida, K.; Gao, J. Gas entrainment characteristics of diesel spray injected by a group-hole nozzle. *Fuel* **2010**, *89*, 3287–3299. [CrossRef]
18. Wadekar, S.; Oevermann, M. Large-eddy simulation study of ultra-high fuel injection pressure on gasoline sprays. *Flow Turbul. Combust.* **2020**. [CrossRef]
19. Chen, X.; Chow, L.; Sehmbey, M. Thickness of film produced by pressure atomizing nozzles. In Proceedings of the 30th AlAA Thermophysics Conference, San Diego, CA, USA, 19–22 June 1995.
20. Benjamin, M.A.; Mansour, A.; Samant, U.G.; Jha, S.; Liao, Y.; Harris, T.; Jeng, S.M. Film thickness, droplet size measurements and correlations for large pressure-swirl atomizers. In *International Gas Turbine & Aeroengine Congress & Exhibition*; American Society of Mechanical Engineers (ASME): Stockholm, Sweden, 1998.
21. Pautsch, A.G.; Shedd, T.A. Adiabatic and diabatic measurements of the liquid film thickness during spray cooling with FC-72. *Int. J. Heat Mass Tran.* **2006**, *49*, 2610–2618. [CrossRef]
22. Alonso, M.; Kay, P.J.; Bowen, P.J.; Gilchrist, R.; Sapsford, S. A laser induced fluorescence technique for quantifying transient liquid fuel films utilising total internal reflection. *Exp. Fluids* **2010**, *48*, 133–142. [CrossRef]
23. Doudou, A.; Maslouhi, A. Macro-microscopic investigation of high-pressure sprays injected by a common rail system. *J. Mech. Sci. Technol.* **2007**, *21*, 1284–1292. [CrossRef]
24. Shams, M.; Naderi, P.; Ashgriz, N. Effect of semicylindrical counter electrodes on the cone-jet mode of electrospray. *At. Sprays* **2020**, *30*, 11–29. [CrossRef]